*J Neurophysiol* 114: 1862–1873, 2015.
First published July 29, 2015; doi:10.1152/jn.00644.2015.

# Maps of interaural delay in the owl's nucleus laminaris

**Catherine E. Carr,[1] Sahil Shah,[1] Thomas McColgan,[2,3] Go Ashida,[1] Paula T. Kuokkanen,[3] Sandra Brill,[2] Richard Kempter,[3] and Hermann Wagner[2]**

[1]*Department of Biology, University of Maryland, College Park, Maryland;* [2]*Institute for Biology II, RWTH Aachen, Aachen, Germany; and* [3]*Institute for Theoretical Biology, Department of Biology, Humboldt-Universität zu Berlin, and Bernstein Center for Computational Neuroscience, Berlin, Germany*

Submitted 29 June 2015; accepted in final form 24 July 2015

**Carr CE, Shah S, McColgan T, Ashida G, Kuokkanen PT, Brill S, Kempter R, Wagner H.** Maps of interaural delay in the owl's nucleus laminaris. *J Neurophysiol* 114: 1862–1873, 2015. First published July 29, 2015; doi:10.1152/jn.00644.2015.—Axons from the nucleus magnocellularis form a presynaptic map of interaural time differences (ITDs) in the nucleus laminaris (NL). These inputs generate a field potential that varies systematically with recording position and can be used to measure the map of ITDs. In the barn owl, the representation of best ITD shifts with mediolateral position in NL, so as to form continuous, smoothly overlapping maps of ITD with iso-ITD contours that are not parallel to the NL border. Frontal space (0°) is, however, represented throughout and thus overrepresented with respect to the periphery. Measurements of presynaptic conduction delay, combined with a model of delay line conduction velocity, reveal that conduction delays can account for the mediolateral shifts in the map of ITD.

local field potential; interaural time difference; auditory; phase; neurophonic

COMPUTATION OF SOUND SOURCE location is a fundamental function of the auditory system. Sound location may be represented in the brain either by place maps, where each neuron in the map has a spatially restricted, narrow receptive field (Konishi 1986), or by more broadly tuned neurons whose firing rate changes with location, and whose maximum responses may even lie outside the physiological range (Baldi and Heiligenberg 1988; Lee and Groh 2014). Recent findings suggest that animals use both coding strategies. In birds and alligators, delay line inputs from each side can form place maps of interaural time difference (ITD) (Carr and Konishi 1990; Carr et al. 2009; Köppl and Carr 2008; Overholt et al. 1992; Seidl et al. 2010), while mammals could achieve ITD sensitivity using changes in rate in broadly tuned neurons (Grothe et al. 2010; Hancock et al. 2010; Joris and Yin 2007; McAlpine et al. 2001). Both approaches are feasible; some birds and mammals localize sound very precisely, resolving ITDs as small as 10–20 $\mu$s (Butts and Goldman 2006; Goodman et al. 2013; Shackleton et al. 2003; Takahashi et al. 2003).

Place maps are the core of the Jeffress model, in which axonal arbors create maps of internal delay that are equal and opposite to the external ITDs. Delay line inputs travel to their target, the nucleus laminaris (NL), in birds and the medial superior olive in mammals and are tapped by an array of binaural coincidence detector neurons. Position within the array determines the best ITD; equal delay inputs from each side correspond to ITDs around 0 $\mu$s, while longer contralateral delays lead to best ITDs in the contralateral hemifield.

How place maps are assembled has been a puzzle. Ordered inputs from the two cochlear nuclei do not necessarily create a map; Karino et al. (2011) reanalyzed axonal projections from labeled and physiologically characterized axons of cat spherical bushy cells that projected to the medial superior olive. The reconstructed axonal arbors looked like delay lines, in that ipsilateral and contralateral projections formed an interdigitating array (Beckius et al. 1999; Smith et al. 1993). Nevertheless, estimated axonal delays could not account for the physiological distribution of best delays and thus do not form a place map (Karino et al. 2011). In the chickens, however, NL contains a place map. Binaural NL neurons receive ipsilateral inputs that splay out to innervate an isofrequency band in NL with approximately equal lengths to each neuron, so that ipsilateral inputs arrive simultaneously along the mediolateral extent of NL. Thus the ipsilateral axons do not act as delay lines. The contralateral axons act as delay lines: each axon runs along the ventral surface of NL, giving off collateral branches along the mediolateral dimension (Köppl and Carr 2008; Overholt et al. 1992; Seidl et al. 2014). Medial NL receives inputs with roughly equal delay from each side, and neurons there are sensitive to ITDs around 0 $\mu$s, while lateral NL maps contralateral ITDs (Köppl and Carr 2008). In summary, in cats, neither input acts as a delay line, while in chickens, only contralateral axons do.

In barn owls, the chicken pattern is extended so that ipsilateral input axons still splay out to innervate NL with approximately equal lengths along each isofrequency band, but then dive into the greatly expanded dorsoventral dimension of barn owl NL, so the ipsilateral axon collaterals travel from dorsal to ventral within the nucleus and interdigitate with axons coming from the contralateral cochlear nucleus. Recordings in NL revealed that both ipsilateral and contralateral collaterals showed a steady shift in phase with recording depth and thus formed maps of ITD within the dorsoventral dimension of NL (Carr and Konishi 1990). Single-cell recordings from NL neurons also showed that best ITDs shifted from contralateral ITDs toward the ipsilateral acoustic field with increasingly ventral position in NL (Peña et al. 2001) in a manner consistent with measured axonal delays (Carr and Konishi 1990). What was missing was how the maps of delay were organized in the mediolateral direction of NL, or the dimension that contains the map of ITD in chickens. Sullivan and Konishi (1986) had proposed that iso-ITD lines were parallel to the dorsal and ventral borders of NL, i.e., the mediolateral dimension contained many equivalent maps of ITD, but our laboratory's

Address for reprint requests and other correspondence: C. E. Carr, Dept. of Biology, Univ. of Maryland, College Park, MD 20742-4415 (e-mail: cecarr@umd.edu).

recent models of axonal delay (McColgan et al. 2014) showed that this interpretation could not be correct.

To reconcile the data on the different maps of ITD, and to determine the role of the axonal arbors from each side, we have measured ITD and conduction delay throughout NL. We used neurophonic responses for this task because they reflect local sensitivity to the ITDs available to the coincidence detector neurons (Bojanowski et al. 1989; Chimento and Schreiner 1990; Henry 1997; Henry and Mulroy 1995; Kuokkanen et al. 2010, 2013; McLaughlin et al. 2010; Schwarz 1992; Snyder and Schreiner 1984; Sullivan and Konishi 1986). Nevertheless, neurophonic origins remain obscure (Goldwyn et al. 2014; Kuokkanen et al. 2010, 2013; McLaughlin et al. 2010). Recordings from chicken NL revealed essentially identical ITD sensitivity for neurophonic and single-unit recordings from NL neurons (Köppl and Carr 2008), and neurophonic potentials may originate from the synaptic currents in both chicken NL and the cat medial superior olive, since they reach their maxima in the vicinity of the densely packed neuron layer (Goldwyn et al. 2014; Köppl and Carr 2008; McLaughlin et al. 2010; Schwarz 1992). Signal-to-noise analyses of the barn owl neurophonic, however, show that the coherent signal from the afferent axons (the delay lines) and their synapses on NL neurons are sufficient to explain the properties of the neurophonic (Kuokkanen et al. 2010). Despite the uncertainty about whether the neurophonic is primarily pre- or postsynaptic, its use has allowed us to measure the interaural delays available to NL neurons and to show how varying conduction delays in the axonal inputs to NL underlie the formation of continuous, smoothly overlapping maps of ITD throughout the nucleus.

## MATERIALS AND METHODS

The experiments were conducted at the Department of Biology of the University Maryland at College Park. Twelve American barn owls of either sex (*Tyto furcata pratincola*, formerly *Tyto alba*) were used to collect the data presented in this study, nine for mapping with lesions at 0 $\mu$s, and three with detailed mapping that included click response measurements at each recording site. Most animals also supplied data for previous publications in Kuokkanen et al. 2010, 2013, McColgan et al. 2014, and Wagner et al. 2005, 2009, and some data were presented at a conference (Carr et al. 2013). Our procedures conform to National Institutes of Health guidelines for animal research and were approved by the animal care and use committee of the University of Maryland. Most animals were used in two or three separate 8-h experiments, spaced approximately 1 wk apart. Anesthesia was induced by intramuscular injections of 16 $mg \cdot k^{-1} \cdot h^{-1}$ ketamine hydrochloride ("Ketavet", Phoenix, St. Joseph, MO) plus 3 $mg \cdot k^{-1} \cdot h^{-1}$ xylazine ("Xyla-ject", Phoenix). Supplementary doses of ketamine and xylazine were administered to maintain a suitable plane of anesthesia. Body temperature was measured by a cloacal probe and kept constant at 39°C by a feedback-controlled heating blanket wrapped around the owl's body (Harvard Instruments, Braintree, MA). An electrocardiogram was used to monitor the plane of anesthesia. In a subset of animals, at the end of the experiment, 0.036 mg buprenorphine hydrochloride ("Buprenex", Reckitt & Colman Products, Richmond, VA) was administered, after which the animal was allowed to recover.

*Surgery and stereotaxis.* Initially, the owl's head was firmly held in a controlled position by a custom-designed setup, using ear bars and a beak holder. Then a metal head plate and short metal pin marking a standardized zero point were permanently glued to the skull. After this, the ear bars and beak holder were removed, and the head held by the head plate alone. An opening was made in the skull around the desired area relative to the zero point, and a small hole was made in the dura mater, taking care to avoid blood vessels. Each electrode was set to zero depth and moved in defined amounts in the rostrocaudal and mediolateral axes, before being advanced into the brain. In some cases, the electrode was angled to facilitate access to the most medial regions of the brain stem.

*Electrodes and recording setup.* Owls were placed on a vibration-insulated table within a sound-attenuating chamber (IAC) that was closed during all recordings. Generally, commercial, Epoxylite-coated tungsten electrodes (Frederick Haer) were used, with impedances between 2 and 20 M$\Omega$ and generally 250-$\mu$m diameter shank (see Fig. 8G in Kuokkanen et al. 2010). A grounded silver chloride pellet, placed under the animal's skin around the incision, served as the reference electrode. Extracellular electrode signals were amplified and filtered by a custom-built headstage and amplifier (mA 2000, Walsh Electronics, Pasadena, CA). Recordings were passed in parallel to an oscilloscope, a threshold discriminator [SD1, Tucker-Davis Technologies (TDT)] and an analog-to-digital converter [DD1 (TDT)] connected to a personal computer via an optical interface [OI (TDT)]. Analog waveforms were saved for offline analysis.

*Stimulus generation and calibration.* Acoustic stimuli were digitally generated by custom-written software ("Xdphys" written in Dr. M. Konishi's laboratory at Caltech, CA) driving a signal-processing board [DSP2 (TDT)]. After passing a digital-to-analog converter [DD1 (TDT)] and an anti-aliasing filter [FT6-2, corner frequency 20 kHz (TDT)], the signals were variably attenuated [PA4 (TDT)], impedance-matched [HB6 (TDT)] and attenuated by an additional fixed amount before being fed to commercial miniature earphones. Two separate channels of signals could be generated, passing through separate channels of associated hardware and driving two separate earphones (Yuin PK2). The earphones were housed in custom-built, calibrated from 100 to 10,000 Hz, closed-sound systems, inserted into the owl's left and right ear canals, respectively. Sound pressure levels were calibrated individually at the start of each experiment, using built-in miniature microphones (Knowles EM3068, Ithasca, IL). In most experiments, the analog stimulus waveforms were saved.

Acoustic stimuli were clicks, noises and tones. All stimuli were digitally created with a sampling rate of about 48 kHz (exact sampling interval 20.8 $\mu$s). Clicks were digitally produced and then processed by the TDT systems. Clicks had a rectangular form (Konishi 1973; Wagner et al. 2005, 2009). Several parameters of the click stimulus could be varied: intensity [maximally 0 dB attenuation, corresponding to 65 dB sound pressure level (SPL) spectrum level at 5 kHz (34-dB SPL overall level)], duration (1–4 samples equivalent to 20.8–83.2 ms), and polarity. A condensation click at 0-dB attenuation and two samples of duration served as a reference. The click stimulus was repeated 128 times. Tone bursts of different frequencies (500- to 10,000-Hz range, 50-to 500-Hz steps) were presented monaurally and binaurally. The duration was 100 ms with 5-ms rise/fall times and a constant starting phase. The tone level was in the range of 20- to 60-dB SPL.

*Recording protocol.* While the electrode was lowered, noise bursts were presented as search stimuli. Once auditory neurophonic responses were discernable, tonal stimuli of varying frequencies were applied from both the ipsi- and contralateral side to judge the position of the electrode. At a given recording site, the following protocol was tested to obtain a data set. To determine best frequency, average rates in response to three to five repetitions of each stimulus were calculated within the stimulus window. This paradigm was chosen to derive isointensity frequency response curves for best frequencies between 2 and 7.5 kHz. Best ITDs were determined using two assumptions. First, that ITD tuning changed continuously with depth. Second, that ITDs at or close to 0 $\mu$s would occur within a penetration (a best ITD of 0 $\mu$s). The best ITDs at the other depths were found following assumption number 1 of continuity. Best ITDs were calculated from responses to either tone bursts presented binaurally at the estimated

best frequency, or to stimulation with noise bursts. The noise had a spectrum between 0.1 and 13 kHz, 5-ms rise/fall times, and duration of 100 ms. The overall level of the noise was between 20 and 60 dB SPL. Each stimulus was repeated three to five times. ITDs generally covered about two periods at the best frequency of a location. The tuning to ITD was judged by a Rayleigh test ($P < 0.05$). Click stimuli of peak pressure 65 dB were used to measure delay. Typically, activity from 10 ms before the click presentation as well as the (driven) activity for 10 ms after the click presentation was stored for 128 repetitions.

*Data analysis.* A brief signal analysis was done during the experiment to determine frequency and ITD tuning. After the experiment, the responses were quantitatively analyzed with custom-written software (MATLAB; BEDS scripts from G. B. Christianson). Frequency and ITD tuning were quantified using the variance of the ongoing neurophonic response. Onset effects were excluded, and we averaged the variance over several trials. We used the variance of the neurophonic as a simple measure to describe how far the voltage is spread around its mean. Only those recording sites with both frequency and ITD tuning (Kuokkanen et al. 2013) were accepted for further analysis. For neurophonic click recordings, the averaged analog response waveform was analyzed as described in Wagner et al. (2005, 2009). Briefly, the waveform was high-pass filtered to exclude components below the best frequency and subsequently fitted with a gammatone function. Fitted waveforms of click responses were detected by our algorithm (amplitude greater than the mean + 2 SDs of the background noise for at least three consecutive data points, see Fig. 5*A*). Click waveforms were measured with a resolution of 20.8 $\mu$s, and ipsi- and contralateral responses were superimposed to determine the click latency difference. The median difference between two to four consecutive maxima and minima was taken as the difference in response latency, with positive values indicating contralateral leading. We recorded from both sides of the brain, with contralateral ear leading ITDs described as negative, and ipsilateral positive. All ITD maps were shown as right-hand side, i.e., left-hand side ITDs were inverted, and data from left- and right-hand side NL combined.

*Electrolytic lesions and histology.* Lesions (10 $\mu$A, 10 s) were made at locations closest to 0 $\mu$s ITD, using a constant-current device (CS3, Transkinetics, Canton, MA). After a survival time of 5–14 days, owls were perfused transcardially with saline, followed by 4% paraformaldehyde in phosphate buffer. Brains were blocked in the same stereotaxic apparatus as for in vivo recordings, then cut either in the same transverse plane as the electrode penetrations or in a plane parallel to the isofrequency axis, which was approximately caudolateral to rostromedial, or at 45° to the transverse plane. Sections were mounted on gelatin-coated slides and stained with cresyl violet. All sections were examined at low magnification to identify electrode tracks and lesions, and then every third section was visualized and reconstructed using a Neurolucida neuron tracing system (Microbrightfield Bioscience, St. Albans, VT) that included an Olympus BX61 light microscope, a video camera (MBF-CX9000, Microbrightfield), a motorized stage controller, and a personal computer. Sections were traced and digitized directly on the microscope using a ×10 objective, with the *Z*-position inputted based on the thickness of each slice. Each section was aligned with the previous slice using rotation, reflection, or translation only. Lesion, lesion tracks, and NL borders were marked using the tracing function. The ruler function was used to measure distances from the lesion center to the borders of the nucleus. The distance of each lesion along its isofrequency band, along an approximately caudomedial to rostrolateral trajectory, was measured from three-dimensional reconstructions of NL (e.g., dashed lines in Fig. 3*B*). Sections were not corrected for shrinkage (Kuokkanen et al. 2013), since measurements were normalized.

*Conduction velocity simulations.* To simultaneously estimate the delay line conduction velocities of the axons inside and outside NL, we implemented a model of axon geometry (McColgan et al. 2014). The model assumed axon geometry of straight-line segments, with different conduction velocities in different regions. This setup allowed latencies measured from click delays and recording locations measured from histology and stereotaxis to be combined in a linear system of equations. The coefficients in this system of equations were given by the axon segment lengths, the delays, and the (unknown) conduction velocities. In general, there were more measurements than unknowns, making the system of equations over-determined. Fits were performed, varying the conduction velocities to reduce the discrepancy between predicted and measured latencies. This discrepancy was quantified using the root mean square (RMS) error and called fitting error. Fitting errors were plotted in a heatmap (not shown) as a function of the velocities, which then showed the best fit and other combinations of velocities that produce low fitting errors. The fitting error may be used as a proxy for the likelihood of the conduction velocity estimation, but since there were uncertainties in both the measurement location and the exact timing, deriving the exact likelihood mathematically was not simple. We found the fitting error to be a suitable intuitive measure of how well the model matched the measurements for a given set of velocities.

## RESULTS

This report is based on 380 extracellular neurophonic recordings within the NL of the barn owl. To reveal the role of conduction velocity in the formation of the maps of ITD, we recorded responses to binaural tones at ITDs within the physiological range, and then measured the latencies of responses to monaural ipsilateral and contralateral clicks. Our physiological ITD maps were later confirmed anatomically by small electrolytic lesions generally at or close to the location where the response to 0 $\mu$s ITD was largest. The results are presented in three sections: *1*) analysis of the ITD sensitive neurophonic potentials in NL that extend a previous study from Sullivan and Konishi (1986); *2*) lesion reconstructions that reveal systematic shifts in the representation of best ITD; and *3*) measurement and simulation of conduction delays to show how the observed microsecond precision is generated from intrinsically noisy elements.

*Analysis of ITD-sensitive local field potentials.* In NL, tone bursts elicited a smooth and nearly sinusoidal evoked potential containing a major spectral component identical to that of the stimulus tone (Fig. 1; Kuokkanen et al. 2010, 2013; Sullivan and Konishi 1986; Wagner et al. 2005). Confirming previous findings, the amplitude of this potential was sensitive to ITD (Köppl and Carr 2008; Kuokkanen et al. 2010, 2013; Schwarz 1992; Sullivan and Konishi 1986). Neurophonic responses tended to be large, typically in the millivolt range (Fig. 1, *B* and *C*), robust, and reliable; essentially identical responses emerge to repetitions when presenting tone bursts. We utilized the power spectral density (Fig. 1*D*) to complement measures of the neurophonic waveform in Fig. 1*C*. Since the second harmonic was much smaller than the large peak at the stimulus frequency, the binaural signal was highly sinusoidal, especially at best ITDs; this sinusoidal waveform of the extracellular signal was similar to intracellularly recorded membrane potential oscillations of NL neurons (Funabiki et al. 2011; Kuokkanen et al. 2013).

To understand the neurophonic's remarkable temporal precision, and to support using it to derive maps of ITD, we developed signal-to-noise ratio analysis methods for direct comparison of experimental data and theory (Ashida et al. 2012; Kuokkanen et al. 2010, 2013). These technical advances suggested the presence of hundreds of sources for the neuro-

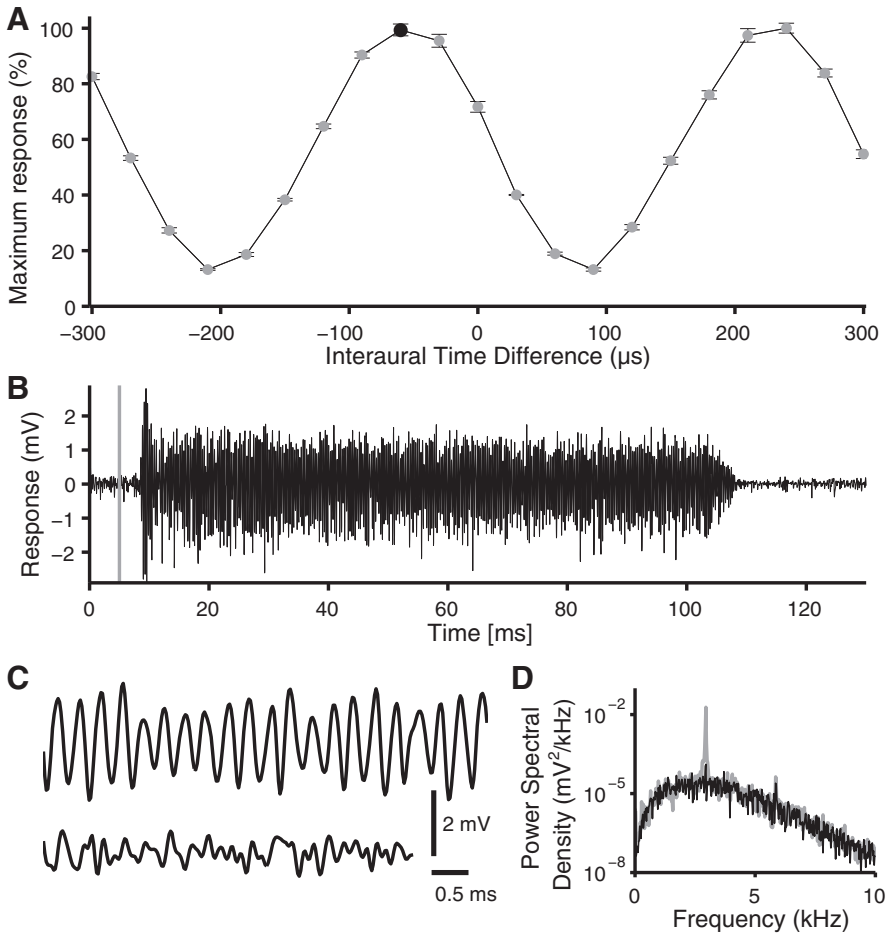


Fig. 1. Interaural time difference (ITD)-sensitive local field potentials in nucleus laminaris (NL). *A*: neurophonic ITD curve with best-frequency tones as the stimulus. Response was obtained from the variance of the sustained activity (onset excluded) ± SE, where 100% corresponds to 0.76 $mV^2$ in this example. Stimulation is at 50 dB; stimulus frequency is 3.5 kHz. *B*: analog recording of the neurophonic response to a 100-ms binaural stimulation at best ITD (black dot in *A*). Neurophonics have 2- to 3-ms latency (stimulus started at 5 ms, gray vertical line) and are highly reproducible. Tick marks are 20 ms apart. *C*: monaural and binaural tone bursts elicited a nearly sinusoidal evoked potential in NL containing a large spectral component identical to that of the stimulus tone. *Top*: recording at best ITD. *Bottom*: recording at worst ITD. *D*: mean power spectral density (PSD) of the driven response. Gray line shows PSD at the best ITD (*B*), based on activity 15–95 ms after the onset of the tone and three stimulus repetitions; note the large peak at the stimulus frequency. Black line shows the PSD for the worst ITD.

phonic, supporting the hypothesis that the neurophonic signal is largely composed of responses from many nucleus magnocellularis (NM) afferent axons and/or synapses onto NL neurons (Kuokkanen et al. 2010, 2013). We, therefore, assumed that the neurophonic was largely generated by the input to NL, and that its sensitivity to ITD reflected the summed potentials from ipsi- and contralateral NM axons and their synapses.

Within NL, the binaurally evoked neurophonic varied with ITD (Fig. 2*A*), as did ITD-sensitive responses recorded from the postsynaptic NL neurons (Carr and Konishi 1990; Funabiki et al. 2011; Peña et al. 1996, 2001; Sullivan and Konishi 1986). The maximum neurophonic responses to best ITD changed systematically with depth, shifting smoothly from contralateral toward ipsilateral ITDs, as the electrode was advanced from dorsal to ventral in a penetration. These location-dependent shifts in best ITD occurred only within NL. Sullivan and Konishi (1986) showed that lesions marking the onset of the systematic shift were found on the dorsal edge of the nucleus, and those marking the end of the phase shift were seen exclusively on the ventral edge (Fig. 2*A*). Note, in the illustrated recording series through left NL, there was no ITD tuning outside NL at a depth of 10,500 $\mu$m (Fig. 2*A*). ITD sensitivity appeared at 10,600 $\mu$m, with a far contralateral peak (around $-120$ $\mu$s, negative ITD by convention). Best ITD shifted smoothly toward 0 $\mu$s ITD (11,150 $\mu$m, red trace) and ITD sensitivity ended at 11,350 $\mu$m with best ITDs in ipsilateral space (around $+90$ $\mu$s).

To test the hypothesis that conduction delays underlaid the systematic shifts in best ITD, we used monaural clicks and measured response latencies, in parallel with measurements of ITD (Fig. 2*B*). Click latencies changed systematically with depth, as the electrode was advanced from dorsal to ventral in a penetration. The click response evoked by stimulation of the left ear (blue trace) led the click response evoked from the right ear (red trace) until a depth of $<$11,250 $\mu$m. Note the ITD closest to 0 $\mu$s was found at 11,150 $\mu$m (red trace in Fig. 2*A*), i.e., the click response closest to 0 $\mu$s ITD was 100 $\mu$m below, possibly because of small movements of tissue in this recording.

*Lesion reconstructions reveal a systematic mediolateral shift in the representation of ITD.* NL is a large nucleus on the dorsal surface of the brain stem, lying below the IVth ventricle (Fig. 3*A*). It is tonotopically organized, with low best frequencies mapped caudal and lateral, and progressively higher frequencies rostral and medial (Carr and Konishi 1990; Takahashi and Konishi 1988a). A band across NL oriented along a diagonal of ~45° to the midline represents a single frequency and will be referred to as an isofrequency band. Isofrequency bands are illustrated as dashed black lines in Fig. 3*B*, which shows a three-dimensional reconstruction of NL and the rostral portion of NM on each side of the brain. Each red dot marked the location of a lesion at 0 $\mu$s ITD of a separate penetration through NL, with best frequencies from 5.6 to 5.8 kHz (left side) and 4.3, 4.5 and 4.8 kHz (right side; note example lesion

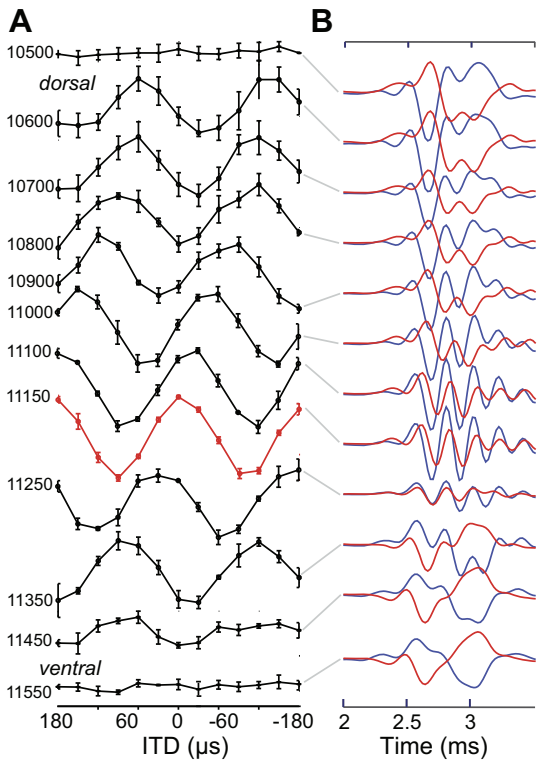


Fig. 2. Responses in NL evoked by binaural tones and monaural clicks. *A*: ITD-sensitive responses were recorded only within NL. Recordings were at mostly 100-$\mu$m intervals through a slightly oblique penetration through left-hand side NL, with depth in $\mu$m. Gray lines link associated monaural click responses in *B* recorded at the same depth. The binaurally evoked neurophonic varied systematically with IPD. Recordings first showed no ITD sensitivity at a depth of 10,500 $\mu$m, then best ITD peaks emerged with a peak in the far contralateral hemifield ($-120$ $\mu$s at 10,600 $\mu$m). Best ITDs shifted toward frontal space (best ITD around 0 $\mu$s at 11,150 $\mu$m; red) and then into ipsilateral space (best ITDs around $+90$ $\mu$s at 11,350 $\mu$m). Some ITD sensitivity remained at 11,450 $\mu$m depth, but ITD did not change between 11,350 and 11,450. *B*: ipsi- (blue, *left*) and contralateral (red, *right*) click responses show a systematic shift in delay with depth. Ipsilateral response extrema occurred earlier in time in dorsal NL, coincided at 11,150 $\mu$m depth, when responses were maximal at 0-$\mu$s ITD, and then occurred later in ventral NL. In most ventral NL (11,350 $\mu$m), note the contralateral extrema led the ipsilateral response. Click responses were averages of 128 click responses, filtered and normalized (Wagner et al. 2005, 2009).

in Fig. 3*A*, arrow). To map best ITD within an isofrequency band, multiple stereotaxically controlled penetrations were made through the overlying cerebellum along or close to the imagined diagonal shown by the dotted black lines in Fig. 3*B*. Generally, electrode penetrations along this diagonal yielded the same or similar best-frequency responses, allowing for deviations around surface blood vessels (i.e., two adjacent penetrations, ~300 $\mu$m apart in right-hand NL, in Fig. 3*B*, had best frequencies of 4.5 and 4.8 kHz, or less than 1/10th octave difference). In lateral NL, measuring systematic changes in frequencies below 3 kHz was more difficult since NL has a lateral bend where frequencies from 500 to 2,000 Hz are represented (Köppl and Carr 1997; Köppl 2001; Takahashi and Konishi 1988b). For frequencies between 3 and 8 kHz, however, NL was so large and ordered that three to four serial penetrations along the same isofrequency band in vivo were possible within an 8-h experimental period. The barn owl's NL is hypertrophied compared with other birds (Kubke et al. 2004), with a volume within its glial borders of 4.8 $\pm$ 1.07 mm$^3$ (mean $\pm$ SD, body weight 468 $\pm$ 36 g, $n = 8$). The measured length of the reconstructed isofrequency bands was 2,738 $\pm$ 522 $\mu$m (mean $\pm$ SD, $n = 8$).

To quantify the distribution of best ITDs within an isofrequency band, we measured the changes in ITD tuning in the neurophonic obtained from traversing the short, dorsoventral axis of NL (Figs. 3*A* and 4). For most penetrations, we then made a lesion at the site corresponding to an ITD of 0 $\mu$s (Fig. 4*A*). We then repeated this sequence at progressively more lateral penetrations along an isofrequency band. Lesions varied in size, from 50- to 230-$\mu$m diameter (mean $\pm$ SD = 118 $\pm$ 47 $\mu$m, $n = 30$); an electrode track was also sometimes visible (Fig. 4*A1*). In all cases the center of the lesion was mapped as a point. In two other owls, whose data were not included in Fig. 4 because their electrode angles were slightly diagonal, rather than orthogonal, to NL borders, lesions were made below NL at the end of the penetration, and the depths of each best ITD were computed as points on a line drawn upward from the reconstructed lesions.

In all penetrations, we found a systematic shift in the representation of 0 $\mu$s ITD from medial to lateral along an isofrequency band (Fig. 4*B*). Lesions made at or near 0 $\mu$s ITD shifted steadily ventral in NL in more lateral penetrations. For example, for the two most medial penetrations, 0 $\mu$s was found within the dorsal portion of NL, i.e., at 82% and 87% of NL depth where 100% of NL depth equaled the dorsal edge of NL. To be able to combine measurements from different animals with small variations in brain size, we normalized the position along an isofrequency band, with 0% being most medial, and 100% most lateral in NL (note mean width of 2,738 $\pm$ 522 $\mu$m). For the measurements of best ITD, we combined results from all isofrequency bands, because the range of ITDs did not change with frequency from 3 to 8 kHz. In summary, the 0-$\mu$s ITD line was not parallel to the dorsal and ventral borders of NL (Fig. 4*B*).

To further quantify the distribution of best ITDs within an isofrequency band, we recorded in sequential penetrations through NL along an isofrequency band, i.e., along a caudomedial to rostrolateral diagonal (refer back to Fig. 3*B*, red symbols). Each isofrequency band contained a map of binaural delays, best illustrated by isodelay contours (Fig. 4*C*, 0-$\mu$s contour shown as horizontal green line).

The range of ITDs mapped in NL changed systematically within each isofrequency band, such that the medial portion of an isofrequency band in NL had a larger representation of ipsilateral ITDs, while the lateral portion had a larger representation of contralateral ITDs. Overall, the ITD range encompassed free-field delays (Hausmann et al. 2009; Keller et al. 1998; Moiseff 1989; Poganiatz and Wagner 2001; von Campenhausen and Wagner 2006), but no single recording through NL, parallel to the delay lines, encompassed the entire ITD range. Instead, the mapped ITD range changed with mediolateral position along an isofrequency slab, such that lesions made at or near 0-$\mu$s ITD shifted steadily ventral in NL in more lateral penetrations (Fig. 4*B*); simply put, iso-ITD lines were not parallel to the dorsal and ventral borders of NL (Fig. 4*C*). Thus the most medial recordings were notable for their representation of frontal and ipsilateral ITDs (Fig. 4*C*). More lateral recordings contained larger representations of contralateral ITDs, with 0 $\mu$s, or frontal space, mapped near the ventral edge of NL (green line in Fig. 4*C*).

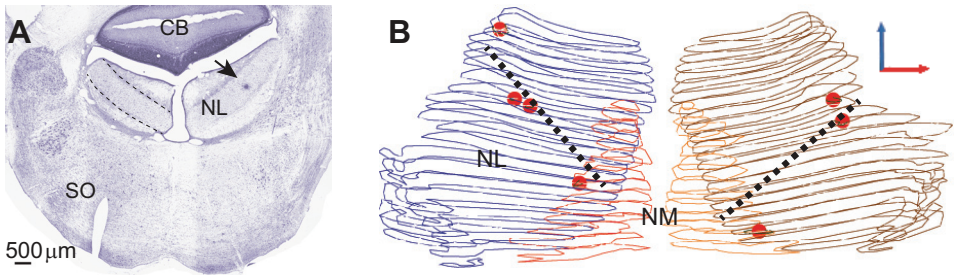


Fig. 3. Lesions mark 0-$\mu$s ITD. *A*: Nissl stained transverse 30-$\mu$m section through barn owl brain stem at the level of central NL. CB, cerebellum; SO, superior olive. The dorsal and ventral borders of NL are outlined by dashed lines along the glial border that surrounds NL, with the tracts made up of nucleus magnocellularis (NM) axons above and below the border. Arrow points to a lesion in central NL at ITD = 0 $\mu$s, 58% along the tonotopic axis, and 40% up from the ventral edge of NL. Notch at *bottom left* marks left-hand side. *B*: three-dimensional reconstruction of NL in an owl where recordings were made from both NLs. The reconstruction has been flattened and is shown from below and includes the rostral portion of NM above NL. Red circles mark lesion locations for recording sites on each side of the brain, and dashed lines indicate isofrequency bands on each side. Rostral NM is shown as orange (*right*) or red (*left*) outlines, while NL is outlined in purple (*left*) or brown (*right*). The arrows at *right* show rotation angle of the reconstruction: red arrow points lateral, blue points rostral, while the dorsal pointing arrow is hidden.

To examine how reproducible the ITD maps were among animals, we examined ITD ranges in NL, by dividing NL into thirds along the isofrequency axis, from medial (0–33% of the isofrequency axis) to central (34–67%) to lateral (68–100%). Three recordings from the medial third of NL revealed ITD range of $-90$ $\mu$s to $+87$ $\mu$s (Fig. 4*C*). In these three medial penetrations, 0 $\mu$s was mapped within the dorsal portion of NL, with ipsilateral space mapped ventrally. A penetration through the most medial edge of NL (7% along the isofrequency band) revealed only best ITDs of 10–75 $\mu$s, while the most lateral penetration in this region (33% along isofrequency band) revealed a larger ITD range ($-90$ to $+87$ $\mu$s, Fig. 4*C*).

The central third of NL contained maps of best ITD centered on frontal and contralateral ITDs, with a total recorded range from $-136$ $\mu$s to $+45$ $\mu$s (Fig. 4, *B* and *C*). Ten penetrations with lesions at 0 $\mu$s were made in the central third of the isofrequency band in 6 owls; four were not completely mapped because we made a lesion at 0 $\mu$s and then did not record at greater depths within NL (note 4 penetrations end at 0 $\mu$s in Fig. 4*C*), while six penetrations through the entire width of NL yielded a mean ITD range of 131 $\pm$ 22 $\mu$s. One hundred thirty-one microseconds represents about 52° and thus covered most of the contralateral ITD range and extended into ipsilateral ITDs. The relation between ITD and azimuth was between 2.5 and 3 $\mu$s/° in the frontal hemisphere (von Campenhausen and Wagner 2006).[1]

The most lateral recordings in any isofrequency band were characterized by representations of contralateral space, with ITDs ranging from $-151$ to $+60$ $\mu$s. Most medially in the lateral portion of NL, at 68% of the isofrequency band, ipsilateral best ITDs around 60 $\mu$s were recorded at the ventral edge of NL (red diamond), while contralateral best ITDs of $-150$ $\mu$s were encountered at the dorsal edge of NL (blue diamond, 80% of the isofrequency band). The most lateral penetration, at 100% of the isofrequency axis (magenta squares), did not even include 0 $\mu$s; it had an ITD range of only $-90$ to $-54$ $\mu$s over 200-$\mu$m depth.

Thus Fig. 4 shows that there was a steady shift in the position of 0 $\mu$s best ITD from dorsal in medial NL to ventral in lateral NL, and no single penetration in NL encompassed the entire range of available ITDs. Instead the ITD range was represented by activity across the whole mediolateral extent of NL. Furthermore, ranges of ITD were highly reproducible among the 10 animals measured.

*Emergence of precise ITD tuning from intrinsically noisy input.* Since the representation of frontal space, i.e., around 0 $\mu$s ITD, shifted systematically to more ventral locations with the progression from medial to lateral along each isofrequency band in NL (Fig. 4), we measured conduction delays, or latencies, at different mediolateral positions at constant sound pressures to determine the basis of the systematic shift, and to show if regulation of conduction velocity could underlie map formation. Because latency in the auditory system increases as best frequency decreases due to cochlear delays, it is important to note that latency was always measured within isofrequency bands, which run from caudomedial to rostrolateral in bird medulla, and not along the tonotopic axis, which is orthogonal to any isofrequency band and runs from caudolateral to rostromedial. Measurements of click latency provided reliable measures of conduction delay (Köppl and Carr 2008; Wagner et al. 2005), because click stimuli were temporally precise. Nevertheless, click stimuli evoked an oscillatory response (Ruggero et al. 1986; Wagner et al. 2005; 2009), in which typically several peaks and troughs (extrema) could be distinguished (Fig. 5*A*).

Neurophonic responses to ipsi- and contralateral clicks at best ITDs at or near 0 $\mu$s generated similar but not identical ipsi- and contralateral click responses, and the latencies of the troughs and peaks of the responses in the individual repetitions coincided (Fig. 5*A*, note overlapping blue and black lines in *inset*). In the example in Fig. 5*A*, the click time difference was 0 $\mu$s, while the associated neurophonic had a best ITD of $-10$ $\mu$s. In what follows, the term "click delay" means the just mentioned time difference between the peaks of the responses evoked by ipsi- and contralateral monaural clicks.

Evoked click delays, measured using monaural clicks, and best ITD, measured in response to binaural stimulation with tones, were generally similar (mean difference = 8.5 $\pm$ 9.9 $\mu$s, $n$ = 17; solid symbols, Fig. 5*B*). Note that our quantitative analyses revealed a temporal jitter of the neurophonic extrema in the range of one or two sampling points that varied from 20.8 to $-41.6$ $\mu$s (see also Wagner et al. 2005). This jitter was small compared with the oscillation periods of about 140–330 $\mu$s considered in this study.

[1] These conversions may overestimate the representation of eccentric space, where 3 $\mu$s/° might be a better fit (von Campenhausen and Wagner 2006).

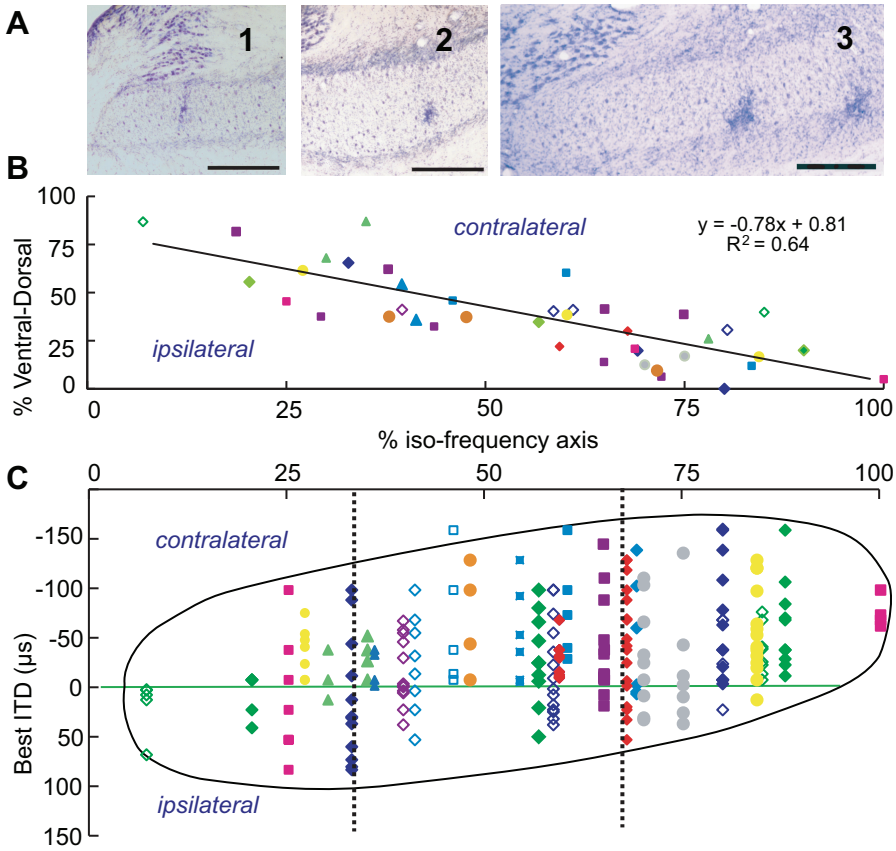


Fig. 4. Dorsoventral maps of ITD revealed by physiological recordings combined with placement of lesions that mark best ITDs near 0 $\mu$s. *A*: examples of lesions used to identify the location of responses to 0-$\mu$s ITD. Nissl-stained right NL, with a portion of NM at *top left* is shown. *A1*: medial lesion (20% along the isofrequency band). *A2*: central lesion (57%). *A3*: two more lateral lesions on the ventral edge of NL (65% and 75% along isofrequency band). Lesions were generated by 10-$\mu$A positive current for 10 s. Bars = 200 $\mu$m. *B*: a shift in the location of lesions revealed a systematic shift in the mapping of frontal space, around 0-$\mu$s ITD. Each data point marks the dorsoventral and isofrequency axis coordinates of a 0-$\mu$s best ITD recording site. The depth of lesions marking 0-$\mu$s ITD in NL increased with increasingly lateral position along an isofrequency band. Ten different symbol colors denote recordings from 10 different animals, while different symbol shapes denote individual penetrations. Left-hand side lesions were reflected onto a right-hand side outline; $n$ = 40 penetrations with confirmed lesions in NL. Note *B* and *C* share a common $x$-axis, marked as %isofrequency axis. *C*: physiological recordings reveal a shift of best ITD with depth. In medial NL, there were more ITDs corresponding to ipsilateral space, while in lateral NL more contralateral ITDs were mapped. Different symbols for different penetrations and animals are as described in *B*. For illustration, best ITDs were plotted surrounded by an outline of NL of dimensions 1:4, i.e., 700 $\mu$m deep, 2,800 $\mu$m wide, and with dashed lines at 33% and 67% of the isofrequency axis. This oval is a guide; note the $y$-axis plots best ITD. Some penetrations were truncated at 0-$\mu$s ITD, while others consisted of only a single ITD measure near 0-$\mu$s ITD, so they are only shown in *B*.

The first peak in the measurement of conduction delay, the signal front delay, was often small and variable (Fig. 5*A*; see Wagner et al. 2005). We therefore measured many click extrema, both positive and negative, occurring after the stimulus presentation. Although the first peak was the most variable, its timing was validated by measurements of later extrema which showed similar click latencies, leading the signal front delay by one or two oscillation cycles; that is, a 2 or 4 $\pi$ phase change. Thus later extrema were generally delayed by multiples of the stimulus period of the best frequency in that region of NL.

To further validate measures of signal front delay, we plotted the latency of first three extrema, including the signal front delay, for four recordings along an isofrequency band (Fig. 6*A*). Although all four recordings were made at the 0-$\mu$s ITD, they showed an increase in click latency with progression along the isofrequency band (Fig. 6*A*, note the slope of each regression was similar). We were then able to use signal front delay to measure latency in a number of recordings, principally to compare our data with recordings from brain slices (Görlich et al. 2010; Overholt et al. 1992; Seidl et al. 2014).

We reasoned that click latency recorded from multiple penetrations along/within the same isofrequency band should provide a measure of mediolateral conduction velocity from the delay line inputs, provided we did not alter sound level (Fig. 6*B*). Minimum absolute latencies should correspond to signal front delays (note that clicks were about 65 dB SPL at 5 kHz). Although identification of signal front delay was intrinsically problematic (see above, and refer back to Fig. 5*A*), because it was smaller than later extrema and had the largest jitter (Carney and Yin 1988; Wagner et al. 2005), in many penetrations ($n$ = 20), we were able to identify the signal front delay in click responses to both ipsilateral and contralateral stimulation. We used these responses to measure absolute latency, i.e., conduction time, to each point marked by a lesion that responded best to sound at 0 $\mu$s ITD (Fig. 6*B*).

These measures of latency were used in a model of NL, which incorporated the geometry of the delay line axons and the measured ITDs (Fig. 7), to determine which combinations of conduction velocities could account for the formation of the maps of ITD (McColgan et al. 2014). This model was able to reproduce the inclined iso-ITD lines observed in the physio-

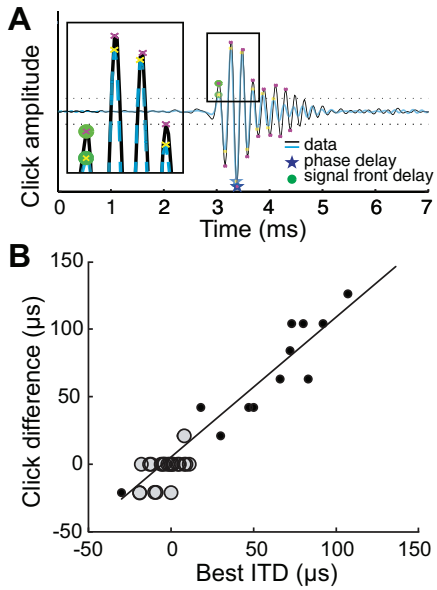


Fig. 5. Neurophonic responses to clicks. *A*: example of click responses close to 0-$\mu$s ITD. Superimposed ipsilateral (cyan) and contralateral (black) data averages of 128 click responses (arbitrary units) from the 5.6-kHz region of NL, with a recording depth of 10,400 $\mu$m are shown. This recording site was in the middle of NL, 57% along the mediolateral axis and 37% along the dorsoventral axis; the best ITD was 8 $\mu$s. *Inset*: enlarged, stretched response from *A* to show measured extrema (yellow and magenta crosses), signal front delay (green circles) and phase delay (blue stars). *B*: click delay differences were correlated with best ITD (4 penetrations with paired click and ITD recordings, linear regression $y = 1.03x + 2.57$, $r^2 = 0.91$, $n = 17$, solid symbols). In most other recordings, click delays were only measured at the lesion site, i.e., closest to 0-$\mu$s ITD (open symbols). ITDs were not all exactly zero; the mean ITD at these sites was $-3.2 \pm 8.8$ $\mu$s, and the mean click delay was $-3.9 \pm 10.7$ $\mu$s, paired *t*-test $P > 0.80$. Note the click measures had a resolution of 20.8 $\mu$s.

logical recordings and allowed for accurate predictions of velocity in both the ipsi- and contralateral axons traveling within NL, and the velocity of the contralateral axons traveling alongside NL (Fig. 7*A*). The model contained several simplifying assumptions; prior to NL, we assumed an initial common pathway and lumped all processes from the auditory periphery to the beginning of the circuit, defined as the medial edge of NL for contralateral processing and the dorsal edge of NL for ipsilateral processing. We also simplified axonal geometries to be straight line segments, so real conduction velocities should be slightly faster.

The model allowed us to estimate axonal velocity, provided that different recording sites in NL were not collinear (this maximizes their information content, see McColgan et al. 2014). As an example, the measurement locations shown in Fig. 7*B* are from two penetrations. If only one penetration were used, measurement locations would be collinear, and the system of equations used in the model would become underdetermined and would be not solvable. Taking more than one point from each of the two penetrations creates a situation in which the points are not collinear, allowing the estimation of all velocities. In experiments on two owls, therefore, we made measurements with a low correlation between measurement locations. To do this, we made oblique penetrations through NL, not parallel to NM axonal delay lines, but at an angle to them, like the penetrations shown as colored dots in Fig. 7. We recorded click delays and best ITDs at 100-$\mu$m intervals in these penetrations through NL (e.g., Fig. 2). Best ITDs at points close to the dorsal edges of NL had large contralateral ITDs (171 and 136 $\mu$s, respectively), while best ITDs close to the ventral edges of NL were in the ipsilateral range of ITDs ($-15$, $-84$ $\mu$s). Simulation of ipsilateral and contralateral delays inside NL yielded straight-line velocities of 5.5 m/s in the dorsoventral dimension, and 11.2 m/s in the mediolateral i.e., below NL, direction. The overall best fit RMS error was 21 $\mu$s (Fig. 7). Previous predictions of iso-ITD lines being more parallel to the dorsal and ventral borders of NL (Sullivan and Konishi 1986) yielded fits with an overall RMS error of 70 $\mu$s, with a conduction velocity in axons below NL of 15 m/s, and conduction velocity within NL of 2 m/s. The worse fit iso-ITD lines subtended an angle of 7° to the border of NL. Thus the model allowed for accurate predictions of axonal velocity, given the two-dimensional geometry of the delay line axons,

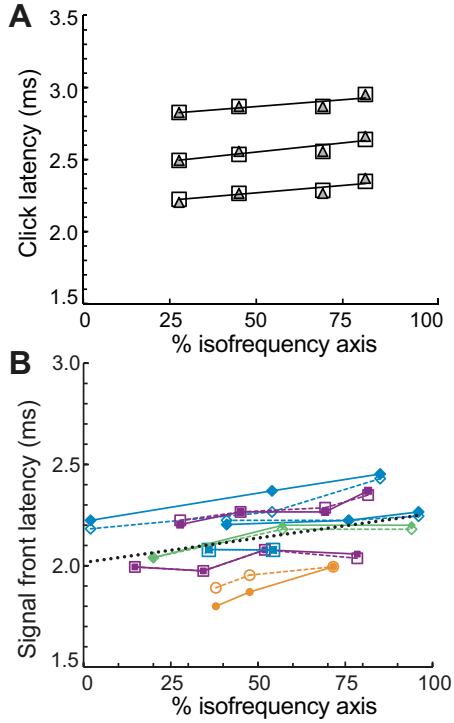


Fig. 6. Measuring latency using clicks. *A*: click extrema were separated by multiples of the inverse of the best frequency and showed a systematic increase in latency with mediolateral position in NL for both ipsi- and contralateral responses. This is illustrated with four penetrations through the 3.6-kHz isofrequency region of NL (also see solid purple squares in *B*) at 28, 45, 69 and 82% of the tonotopic axis. The latencies of the first three click extrema, including the signal front delay, are shown. Linear regression lines drawn through ipsilateral extrema (triangles) were $y1 = 0.0019$ ms/% $x + 2.761$ ms ($r^2 = 0.76$), $y2 = 0.0025$ ms/% $x + 2.426$ ms ($r^2 = 0.78$), $y3 = 0.0020$ ms/% $x + 2.167$ ms ($r^2 = 0.90$). Contralateral extrema (squares) were similar to ipsilateral extrema. *B*: signal front delays were used to provide a measure of latency and plotted with respect to the isofrequency axis, i.e., from caudomedial (0%) to rostrolateral (100%), for the 7 cases in which the signal front delays in a penetration series where both peaks (ipsi and contra) were positive. Despite being intrinsically noisy (see text), signal front delays showed a systematic increase in latency with mediolateral position, for recordings from both ipsilateral (open symbols, dashed lines) and contralateral units (solid symbols, solid lines, same colors as Fig. 4, *B* and *C*). To normalize for latency changes with frequency, we calculated a regression through all points and set the midpoint of each line to 50% of tonotopic axis, with 2-ms latency. This yielded a linear regression $y = 0.0019$ ms/% $x + 1.88$ ms, $r^2 = 0.58$. The linear regression without this normalization was $y = 0.0024$ ms/% $x + 2.016$ ms, $r^2 = 0.17$ (dotted line).

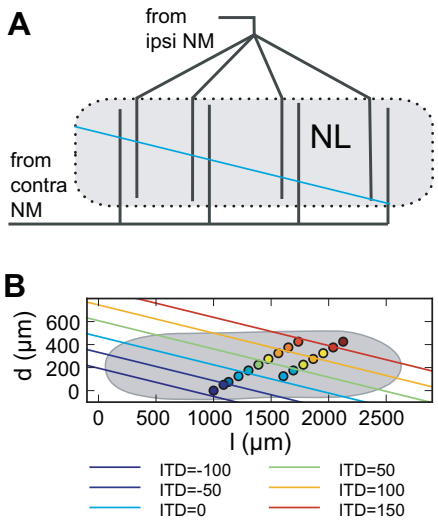


Fig. 7. Multivariate regression analyses of conduction velocity. *A*: schematic NL outline showing modeled straight-line axon segment lengths, ipsilateral inside NL, contralateral inside NL and contralateral outside NL. A model of these axons (McColgan et al. 2014) allowed us to combine distances and conduction velocities to predict ITDs. Aqua line in *A* and *B* marks predicted 0-$\mu$s iso-ITD line. *B*: diagram of NL dorsal (*d*) and length (*l*) dimensions with the best model fit for measured ITDs (colored dots) with predicted iso-ITD lines. Measurement locations were drawn as circles at their dorsoventral (*d*, *x*-axis) and mediolateral (*l*, *y*-axis) location within NL. Iso-ITD lines resulting from the best fit conduction velocities are in the same color. Note iso-ITD lines were not parallel to the border of NL.

and was able to reproduce the inclined iso-ITD lines observed in the physiological recordings.

In summary, neurophonic recordings in NL revealed smoothly shifting maps of best ITD, created by precisely regulated conduction delays.

## DISCUSSION

ITDs are behaviorally important for sound source localization, and in birds are first computed in NL. We have shown here how ITD is represented in the inputs to NL, and how conduction delays create temporally precise maps of ITD. A key assumption of this study is that the postsynaptic coincidence detector neurons in NL act as point sources to tap into the presynaptic maps (Funabiki et al. 2011; Peña et al. 2001). This assumption is supported by the short dendrites of the coincidence detectors (Carr and Boudreau 1993; Carr and Konishi 1990), and by the observation that ITD responses recorded from NL neurons change systematically with depth, consistent with maps of delay (Peña et al. 2001).

*Distribution of best delays and the formation of maps of ITD in the barn owl.* In barn owl NL, the NM axonal segments traveling through NL provide the delay required for creating maps of contralateral and frontal ITDs (Carr and Boudreau 1993; Carr and Konishi 1990). Unlike most birds (Kubke and Carr 2006), barn owl NL is organized in two dimensions, allowing for multiple representations of azimuthal space within each isofrequency band. Within the isofrequency bands in NL, the representation of best ITD shifts systematically, forming a single continuous map of ITD, with frontal ITDs (around 0°) represented throughout. Barn owls are auditory predators that fixate their targets prior to strike (Konishi 1973), and the consistent representation of frontal space may be an adaptation to a predatory life style and frontally directed eyes.

Best ITDs are maintained in the projections of NL neurons to the core region of the central nucleus of the inferior colliculus (IC) (Takahashi et al. 1987; Takahashi and Konishi 1988a). There, the spatially extended map of ITD from NL converges upon a single ITD map in each isofrequency lamina (Wagner et al. 1987). This convergence should improve the precision of the representation of frontal ITDs. The NL recipient zone in the core receives a crossed projection from the largely contralateral map in NL, thus forming a representation of the ipsilateral hemifield (Wagner et al. 1987, 2002). It is not known whether the ipsilateral ITDs we found in NL cross to form a contralateral representation in the core, or whether they project to the ipsilateral IC. The neurons of the core project across the IC to the contralateral lateral shell, where they form a representation of the contralateral hemifield (Takahashi et al. 1989; Wagner et al. 1987). Feldman and Knudsen (1997, their Fig. 2) reported a representation of azimuthal space in the IC lateral shell from 15° ipsilateral to 80° contralateral, suggesting that an ipsilateral component is present, potentially relayed from NL via the core, or as a direct projection from ipsilateral NL. Either is possible; the axons from the most medial "ipsilateral" representation in NL might not cross in the lateral lemniscus, since lemniscal pathways are not generally totally crossed. In chickens and zebra finches, for example, ipsilateral projections are present (Conlee and Parks 1986; Krützfeldt et al. 2010; Wang and Karten 2010). The data available for the owl do not exclude these various possibilities (Konishi 1986; Takahashi and Konishi 1988a).

The lateral shell projects to the external nucleus, or space map, which in turn projects to the optic tectum. In general, responses to frontal locations are over-represented in both the external nucleus and the optic tectum (Knudsen 1982; Olsen et al. 1989), consistent with over-representation of frontal space in the two NLs. The barn owl's behavioral focus on frontal space is also reflected in the distribution of ITD-sensitive forebrain sites (Cohen and Knudsen 1995, 1998; Knudsen et al. 1991; Olsen et al. 1989; Vonderschen and Wagner 2009, 2012). Despite the robust representation of frontal space, however, information from the eccentric loci mapped in NL must be maintained in the IC, since Cazettes et al. (2014) found neurons tuned to locations as lateral as 100° azimuth in the external nucleus.

*Role of delay in the formation of maps of ITD.* Computation of ITD requires precise temporal coding. How the required precision is achieved is an unresolved question. Several steps are necessary: the periphery encodes the stimulus, then monaural inputs from the left and right sides carry relative timing information to the coincidence detectors, which respond best when the phase locked input signals from the two ear arrive simultaneously. Delays therefore play an important role in the representation of ITD, since they are necessary for coincidence detection. Delays are also typically asymmetrical, leading to neurons with best sensitivity in the contralateral hemifield and a small part of the ipsilateral hemifield (Bremen and Joris 2013; Franken et al. 2014; Jercog et al. 2010; McAlpine et al. 2001; Myoga et al. 2014; Pecka et al. 2008).

Coincidence detection requires that delays be precise, but they may also be multifaceted (Joris and Yin 2007) and vary among vertebrate groups. Multiple potential sources of delay have been identified, including the conduction delays described here, and cochlear delays or stereausis (Shamma et al. 1989).

In barn owls, stereausis has been ruled out as a source of interaural delays (Peña et al. 2001), but may contribute to delays in cats (Joris et al. 2006). A recent study in gerbils shows that coincidence detection is adaptive, rather than instantaneous, such that the interaction of intrinsic conductances with synaptic activity can generate internal delay as an intrinsic part of the process of coincidence detection (Franken et al. 2014; Myoga et al. 2014; Zhou et al. 2005). Birds and mammals may also employ different strategies for generating conduction delays. In mammals, axonal projections from the cochlear nuclei cannot account for the frequency-dependent distribution of best delays ITDs (Beckius et al. 1999; Karino et al. 2011; Smith et al. 1993), while axonal projections from NM to NL form maps of ITD in birds (Carr and Konishi 1990; Köppl and Carr 2008; Overholt et al. 1992; Seidl et al. 2014). Delays are still precisely encoded in mammals, however, and best ITDs can be predicted from the phase delay of the monaural responses (Bremen and Joris 2013; Day and Semple 2011; Goldberg and Brown 1969; Grothe and Park 1998; Pecka et al. 2008; Spitzer and Semple 1995; Sullivan and Konishi 1986; Yin and Chan 1990). The advantages and disadvantages of ITD maps have been addressed elsewhere insofar as they relate to neural coding strategies (Butts and Goldman 2006; Franken et al. 2014; Harper and McAlpine 2004; Köppl and Carr 2008).

In barn owls and chickens, NM projections to NL create delays to form maps of ITD within each isofrequency lamina (Carr and Konishi 1990; Overholt et al. 1992; Seidl et al. 2014), with conduction delays similar to the range of ITDs available to each bird (Hyson et al. 1994; Köppl and Carr 2008; Moiseff 1989; von Campenhausen and Wagner 2006). Evidence for delay lines is good in the chicken and emu, which show systematic shifts in the conduction time of contralateral NM afferents in vitro (Görlich et al. 2010; MacLeod et al. 2006; Overholt et al. 1992; Seidl et al. 2014) and in vivo (Carr and Konishi 1990; Köppl and Carr 2008; Sullivan and Konishi 1986). In chicken, ipsilateral projections do not appear to act as delay lines (Köppl and Carr 2008; McColgan et al. 2014; Overholt et al. 1992; Seidl et al. 2014). Contralateral axons do act as delay lines and are sufficient to create maps of ITD (Köppl and Carr 2008; McColgan et al. 2014; Overholt et al. 1992). By contrast, in the barn owl, both ipsilateral and contralateral axons create delays. Within NL, ipsilateral response phases increase, and the contralateral response phases decrease, when an electrode is advanced from dorsal to ventral in NL (Carr and Konishi 1988). Furthermore, outside NL, the main "trunk" axons above and below the nucleus show mediolateral increases in delay. Thus, in barn owls, both NM axons show systematic changes in latency inside and outside NL, increasing the number of points where the circuit could be adjusted during development (McColgan et al. 2014). Our model of input axon conduction velocities shows how measured conduction delays could account for the smoothly overlapping shift in the map of ITD with progression from medial to lateral along an isofrequency band.

There are several mechanisms that could underlie the regulation of delay and map formation. We hypothesize that NM axons provide the required delays within the spatial limits of the dorsoventral span of the nucleus, via reductions of internodal distance and axonal diameter, which result in slower conduction velocity within NL. Delayed myelination of axonal segments has been proposed as a mechanism by which internodal distances are reduced (Carr 1995; Cheng and Carr 2007; Pajevic et al. 2014; Seidl 2014). Seidl and colleagues (Fischer and Seidl 2014; Seidl 2014; Seidl et al. 2014) have addressed mechanisms for matching delays, given the obvious path length differences between ipsilateral and contralateral axons. They found contralateral NM axons were longer than their ipsilateral counterparts, although delays were well matched (Köppl and Carr 2008; McColgan et al. 2014). Thus the anatomical restrictions imposed by axonal length may be overcome by variations in axon parameters, allowing isochronic inputs (i.e., close to 0-$\mu$s delay) in NL (Görlich et al. 2010; Overholt et al. 1992; Seidl et al. 2014).

We can predict conduction velocities for the simple one-dimensional chicken case (McColgan et al. 2014). Predictions are more complex for the two-dimensional barn owl NL, where conduction velocities appear to differ between the main trunk axons and the axons that interdigitate within NL. Nevertheless, our model predicted pairs of conduction velocities to account for the smoothly shifting measured maps of ITD (McColgan et al. 2014). Earlier claims, of iso-ITD lines running parallel to the dorsal and ventral borders of NL in the mediolateral direction (Sullivan and Konishi 1986), required biologically unrealistic conduction velocities. Our new data have revealed that isodelay contours are not parallel, but shift systematically from dorsal locations in medial NL to ventral locations in lateral NL, with only frontal azimuth represented throughout. Both model and physiology yielded a range of possible conduction velocities, with velocities in NL being smaller than those outside NL, and velocities in NL of about 6.4 m/s, consistent with previous estimates of 3–5 m/s (Carr and Konishi 1990; McColgan et al. 2014). Candidate mechanisms to regulate the "fine" tuning of delays suggest possible directions for further study. One interesting direction would be to connect synaptic plasticity to the regulation of conduction velocity in NL, as suggested in earlier theoretical papers (Gerstner et al. 1996; Kempter et al. 1999).

## ACKNOWLEDGMENTS

We thank Terry Takahashi for helpful discussion.

Present addresses: S. Shah, Dept. of Neuroscience, University of California, San Diego, La Jolla, CA; G. Ashida, Cluster of Excellence "Hearing4all", University of Oldenburg, Oldenburg, Germany.

## GRANTS

This research was sponsored by National Institute on Deafness and Other Communications Disorders (NIDCD) Grant DC-00436 to C. E. Carr; by NIDCD Grant P30 DC-04664 to the University of Maryland Center for the Comparative and Evolutionary Biology of Hearing; by the German Research Foundation (DFG, Wa-606/12) and the Bundesministerium für Bildung und Forschung (BMBF, Bernstein Collaboration Temporal Precision, 01GQ07101 to H. Wagner and 01GQ07102 to R. Kempter; Bernstein Center for Computational Neuroscience Berlin, 01GQ1001A; Bernstein Focus "Neuronal Basis of Learning", 01GQ0972); and by the cluster of Excellence, "Hearing4all" at the University of Oldenburg (G. Ashida).

## DISCLOSURES

No conflicts of interest, financial or otherwise, are declared by the author(s).

## AUTHOR CONTRIBUTIONS

Author contributions: C.E.C. and H.W. conception and design of research; C.E.C., G.A., and H.W. performed experiments; C.E.C., S.S., T.M., G.A.,

P.T.K., S.B., and R.K. analyzed data; C.E.C., S.S., T.M., and H.W. interpreted results of experiments; C.E.C., S.S., T.M., and P.T.K. prepared figures; C.E.C. drafted manuscript; C.E.C., R.K., and H.W. edited and revised manuscript; C.E.C. approved final version of manuscript.

## REFERENCES


**Ashida G, Funabiki K, Kuokkanen PT, Kempter R, Carr CE.** Signal-to-noise ratio in the membrane potential of the owl's auditory coincidence detectors. *J Neurophysiol* 108: 2837–2845, 2012.

**Baldi P, Heiligenberg W.** How sensory maps could enhance resolution through ordered arrangements of broadly tuned receivers. *Biol Cybern* 59: 313–318, 1988.

**Beckius GE, Batra R, Oliver DL.** Axons from anteroventral cochlear nucleus that terminate in medial superior olive of cat: observations related to delay lines. *J Neurosci* 19: 3146–3161, 1999.

**Bojanowski T, Hu K, Schwarz D.** Analogue signal representation in the medial superior olive of the cat. *J Otolaryngol* 18: 3–9, 1989.

**Bremen P, Joris PX.** Axonal recordings from medial superior olive neurons obtained from the lateral lemniscus of the chinchilla (*Chinchilla laniger*). *J Neurosci* 33: 17506–17518, 2013.

**Butts DA, Goldman MS.** Tuning curves, neuronal variability, and sensory coding. *PLoS Biol* 4: e92, 2006.

**Carney LH, Yin TCT.** Temporal coding of resonances by low-frequency auditory nerve fibers: single-fiber responses and a population model. *J Neurophysiol* 60: 1653–1677, 1988.

**Carr CE.** The development of nucleus laminaris in the barn owl. In: *Advances in Hearing Research, Proceedings of the 10th International Symposium on Hearing*, edited by Manley GA, Klump GM, Köppl C, Fastl H, Oekinghaus H. Hackensack, NJ: World Scientific, 1995, p. 24–31.

**Carr CE, Boudreau RE.** Organization of the nucleus magnocellularis and the nucleus laminaris in the barn owl: encoding and measuring interaural time differences. *J Comp Neurol* 334: 337–355, 1993.

**Carr CE, Konishi M.** Axonal delay lines for time measurement in the owl's brainstem. *Proc Natl Acad Sci U S A* 85: 8311–8315, 1988.

**Carr CE, Konishi M.** A circuit for detection of interaural time differences in the brain stem of the barn owl. *J Neurosci* 10: 3227–3246, 1990.

**Carr CE, Shah S, Ashida G, McColgan T, Wagner H, Kuokkanen PT, Kempter R, Köppl C.** Maps of ITD in the nucleus laminaris of the barn owl. *Adv Exp Med Biol* 787: 215–222, 2013.

**Carr CE, Soares D, Smolders J, Simon JZ.** Detection of interaural time differences in the alligator. *J Neurosci* 29: 7978–7990, 2009.

**Cazettes F, Fischer BJ, Peña JL.** Spatial cue reliability drives frequency tuning in the barn owl's midbrain. *Elife* 3: e04854, 2014.

**Cheng SM, Carr CE.** Functional delay of myelination of auditory delay lines in the nucleus laminaris of the barn owl. *Dev Neurobiol* 67: 1957–1974, 2007.

**Chimento TC, Schreiner CE.** Time course of adaptation and recovery from adaptation in the cat auditory-nerve neurophonic. *J Acoust Soc Am* 88: 857–864, 1990.

**Cohen YE, Knudsen EI.** Binaural tuning of auditory units in the forebrain archistriatal gaze fields of the barn owl: local organization but no space map. *J Neurosci* 15: 5152–5168, 1995.

**Cohen YE, Knudsen EI.** Representation of binaural spatial cues in field L of the barn owl forebrain. *J Neurophysiol* 79: 879–890, 1998.

**Conlee JW, Parks TN.** Origin of ascending auditory projections to the nucleus mesencephalicus lateralis pars dorsalis in the chicken. *Brain Res* 367: 96–113, 1986.

**Day ML, Semple MN.** Frequency-dependent interaural delays in the medial superior olive: implications for interaural cochlear delays. *J Neurophysiol* 106: 1985–1999, 2011.

**Feldman D, Knudsen EI.** An anatomical basis for visual calibration of the auditory space map in the barn owl's midbrain. *J Neurosci* 17: 6820–6837, 1997.

**Fischer BJ, Seidl AH.** Resolution of interaural time differences in the avian sound localization circuit-a modeling study. *Front Comput Neurosci* 8: 99–108, 2014.

**Franken TP, Bremen P, Joris PX.** Coincidence detection in the medial superior olive: mechanistic implications of an analysis of input spiking patterns. *Front Neural Circuits* 8: 42, 2014.

**Funabiki K, Ashida G, Konishi M.** Computation of interaural time difference in the owl's coincidence detector neurons. *J Neurosci* 31: 15245–15256, 2011.

**Gerstner W, Kempter R, van Hemmen JL, Wagner H.** A neuronal learning rule for sub-millisecond temporal coding. *Nature* 383: 76–81, 1996.

**Goldberg JM, Brown PB.** Response of binaural neurons of dog superior olivary complex to dichotic tonal stimuli: some physiological mechanisms of sound localization. *J Neurophysiol* 32: 613–636, 1969.

**Goldwyn JH, Mc Laughlin M, Verschooten E, Joris PX, Rinzel J.** A model of the medial superior olive explains spatiotemporal features of local field potentials. *J Neurosci* 34: 11705–11722, 2014.

**Goodman DFM, Benichoux V, Brette R.** Decoding neural responses to temporal cues for sound localization. *Elife* 2: e01312, 2013.

**Görlich A, Illy M, Friauf E, Wagner H, Luksch H, Löhrke S.** Development of the delay lines in the nucleus laminaris of the chicken embryo revealed by optical imaging. *Neuroscience* 168: 564–572, 2010.

**Grothe B, Park TJ.** Sensitivity to interaural time differences in the medial superior olive of a small mammal, the Mexican free-tailed bat. *J Neurosci* 18: 6608–6622, 1998.

**Grothe B, Pecka M, McAlpine D.** Mechanisms of sound localization in mammals. *Physiol Rev* 90: 983–1012, 2010.

**Hancock KE, Noel V, Ryugo DK, Delgutte B.** Neural coding of interaural time differences with bilateral cochlear implants: effects of congenital deafness. *J Neurosci* 30: 14068–14079, 2010.

**Harper NS, McAlpine D.** Optimal neural population coding of an auditory spatial cue. *Nature* 430: 682–686, 2004.

**Hausmann L, von Campenhausen M, Endler F, Singheiser M, Wagner H.** Improvements of sound localization abilities by the facial ruff of the barn owl (Tyto alba) as demonstrated by virtual ruff removal. *PLos One* 4: e7721, 2009.

**Henry KR.** Auditory nerve neurophonic tuning curves produced by masking of round window responses. *Hear Res* 104: 167–176, 1997.

**Henry WR, Mulroy MJ.** Afferent synaptic changes in auditory hair cells during noise-induced temporary threshold shift. *Hear Res* 84: 81–90, 1995.

**Hyson RL, Overholt EM, Lippe WR.** Cochlear microphonic measurements of interaural time differences in the chick. *Hear Res* 81: 109–118, 1994.

**Jercog PE, Svirskis G, Kotak VC, Sanes DH, Rinzel J.** Asymmetric excitatory synaptic dynamics underlie interaural time difference processing in the auditory system. *PLoS Biol* 8: e1000406, 2010.

**Joris P, Yin TCT.** A matter of time: internal delays in binaural processing. *Trends Neurosci* 30: 70–78, 2007.

**Joris PX, Van de Sande B, Louage DH, van der Heijden M.** Binaural and cochlear disparities. *Proc Natl Acad Sci U S A* 103: 12917–12922, 2006.

**Karino S, Smith PH, Yin TCT, Joris PX.** Axonal branching patterns as sources of delay in the mammalian auditory brainstem: a re-examination. *J Neurosci* 31: 3016–3031, 2011.

**Keller CH, Hartung K, Takahashi TT.** Head-related transfer functions of the barn owl: measurement and neural responses. *Hear Res* 118: 13–34, 1998.

**Kempter R, Gerstner W, van Hemmen JL.** Hebbian learning and spiking neurons. *Phys Rev E Stat Phys Plasmas Fluids Relat Interdiscip Topics* 59: 4498–4514, 1999.

**Knudsen EI.** Auditory and visual maps of space in the optic tectum of the owl. *J Neurosci* 9: 1177–1194, 1982.

**Knudsen EI, Esterly SD, du Lac S.** Stretched and upside-down maps of auditory space in the optic tectum of blind-reared owls; acoustic basis and behavioral correlates. *J Neurosci* 11: 1727–1747, 1991.

**Konishi M.** How the owl tracks its prey: experiments with trained barn owls reveal how their acute sense of hearing enables them to catch prey in the dark. *Am Sci* 61: 414–424, 1973.

**Konishi M.** Centrally synthesized maps of sensory space. *Trends Neurosci* 9: 163–168, 1986.

**Köppl C.** Frequency tuning and spontaneous activity in the auditory nerve and cochlear nucleus magnocellularis of the barn owl Tyto alba. *J Neurophysiol* 77: 364–377, 1997.

**Köppl C.** Tonotopic projections of the auditory nerve to the cochlear nucleus angularis in the barn owl. *J Assoc Res Otolaryngol* 2: 41–53, 2001.

**Köppl C, Carr CE.** Low-frequency pathway in the barn owl's auditory brainstem. *J Comp Neurol* 378: 265–282, 1997.

**Köppl C, Carr CE.** Maps of interaural time difference in the chicken's brainstem nucleus laminaris. *Biol Cybern* 98: 541–559, 2008.

**Krützfeldt NOE, Logerot P, Kubke MF, Wild JM.** Connections of the auditory brainstem in a Songbird, *Taeniopygia guttata*. I. Projections of nucleus angularis and nucleus laminaris to the auditory torus. *J Comp Neurol* 518: 2109–2134, 2010.

**Kubke MF, Carr CE.** Morphological variation in the nucleus laminaris of birds. *Int J Comp Psychol* 19: 83–97, 2006.

**Kubke MF, Massoglia D, Carr CE.** Bigger brains or bigger nuclei? Regulating the size of auditory structures in birds. *Brain Behav Evol* 63: 169–180, 2004.

**Kuokkanen PT, Ashida G, Carr CE, Wagner H, Kempter R.** Linear summation in the barn owl's brainstem underlies responses to interaural time differences. *J Neurophysiol* 110: 117–130, 2013.

**Kuokkanen PT, Wagner H, Ashida G, Carr CE, Kempter R.** On the origin of the extracellular field potential in the nucleus laminaris of the barn owl (*Tyto alba*). *J Neurophysiol* 104: 2274–2290, 2010.

**Lee J, Groh JM.** Different stimuli, different spatial codes: a visual map and an auditory rate code for oculomotor space in the primate superior colliculus. *PLoS One* 9: e85017, 2014.

**MacLeod KM, Soares D, Carr CE.** Interaural timing difference circuits in the auditory brainstem of the emu (*Dromaius novaehollandiae*). *J Comp Neurol* 495: 185–201, 2006.

**McAlpine D, Jiang D, Palmer AR.** A neural code for low-frequency sound localization in mammals. *Nat Neurosci* 4: 396–401, 2001.

**McColgan T, Shah S, Köppl C, Carr CE, Wagner H.** A functional circuit model of interaural time difference processing. *J Neurophysiol* 112: 2850–2864, 2014.

**McLaughlin M, Verschooten E, Joris PX.** Oscillatory dipoles as a source of phase shifts in field potentials in the mammalian auditory brainstem. *J Neurosci* 30: 13472–13487, 2010.

**Moiseff A.** Binaural disparity cues available to the barn owl for sound localization. *J Comp Physiol A* 164: 629–636, 1989.

**Myoga MH, Lehnert S, Leibold C, Felmy F, Grothe B.** Glycinergic inhibition tunes coincidence detection in the auditory brainstem. *Nat Commun* 5: 3790, 2014.

**Olsen JF, Knudsen EI, Esterly SD.** Neural maps of interaural time and intensity differences in the optic tectum of the barn owl. *J Neurosci* 9: 2591–2605, 1989.

**Overholt EM, Rubel EW, Hyson RL.** A circuit for coding interaural time differences in the chick brainstem. *J Neurosci* 12: 1698–1708, 1992.

**Pajevic S, Basser PJ, Fields RD.** Role of myelin plasticity in oscillations and synchrony of neuronal activity. *Neuroscience* 276: 135–147, 2014.

**Pecka M, Brand A, Behrend O, Grothe B.** Interaural time difference processing in the mammalian medial superior olive: the role of glycinergic inhibition. *J Neurosci* 28: 6914–6925, 2008.

**Peña JL, Viete S, Albeck Y, Konishi M.** Tolerance to sound intensity of binaural coincidence detection in the nucleus laminaris of the owl. *J Neurosci* 16: 7046–7054, 1996.

**Peña JL, Viete S, Funabiki K, Saberi K, Konishi M.** Cochlear and neural delays for coincidence detection in owls. *J Neurosci* 21: 9455–9459, 2001.

**Poganiatz I, Wagner H.** Sound-localization experiments with barn owls in virtual space: influence of broadband interaural level different on head-turning behavior. *J Comp Physiol A* 187: 225–233, 2001.

**Ruggero M, Robles L, Rich N, Costalupes J.** Basilar membrane motion and spike initiation in the cochlear nerve. In: *Auditory Frequency Selectivity* (119th Ed.), edited by Moore BCJ, Patterson RD. New York: Springer, 1986, p. 189–198.

**Schwarz DW.** Can central neurons reproduce sound waveforms? An analysis of the neurophonic potential in the laminar nucleus of the chicken. *J Otolaryngol* 21: 30–38, 1992.

**Seidl AH.** Regulation of conduction time along axons. *Neuroscience* 276: 126–134, 2014.

**Seidl AH, Rubel EW, Barría A.** Differential conduction velocity regulation in ipsilateral and contralateral collaterals innervating brainstem coincidence detector neurons. *J Neurosci* 34: 4914–4919, 2014.

**Seidl AH, Rubel EW, Harris DM.** Mechanisms for adjusting interaural time differences to achieve binaural coincidence detection. *J Neurosci* 30: 70–80, 2010.

**Shackleton T, Skottun B, Arnott RH, Palmer A.** Interaural time difference discrimination thresholds for single neurons in the inferior colliculus of guinea pigs. *J Neurosci* 23: 716–724, 2003.

**Shamma SA, Shen NM, Gopalaswamy P.** Stereausis: binaural processing without neural delays. *J Acoust Soc Am* 86: 989–1006, 1989.

**Smith PH, Joris PX, Yin TCT.** Projections of physiologically characterized spherical bushy cell axons from the cochlear nucleus of the cat: evidence for delay lines to the medial superior olive. *J Comp Neurol* 331: 245–260, 1993.

**Snyder R, Schreiner CE.** The auditory neurophonic: basic properties. *Hear Res* 15: 261–280, 1984.

**Spitzer MW, Semple MN.** Neurons sensitive to interaural phase disparity in gerbil superior olive: diverse monaural and temporal response properties. *J Neurophysiol* 73: 1668–1690, 1995.

**Sullivan WE, Konishi M.** Neural map of interaural phase difference in the owl's brainstem. *Proc Natl Acad Sci U S A* 83: 8400–8404, 1986.

**Takahashi TT, Bala ADS, Spitzer MW, Euston DR, Spezio ML, Keller CH.** The synthesis and use of the owl's auditory space map. *Biol Cybern* 89: 378–387, 2003.

**Takahashi TT, Carr CE, Brecha N, Konishi M.** Calcium binding protein-like immunoreactivity labels the terminal field of nucleus laminaris of the barn owl. *J Neurosci* 7: 1843–1856, 1987.

**Takahashi TT, Konishi M.** Projections of the cochlear nuclei and nucleus laminaris to the inferior colliculus of the barn owl. *J Comp Neurol* 274: 190–211, 1988a.

**Takahashi TT, Konishi M.** Projections of nucleus angularis and nucleus laminaris to the lateral lemniscal nuclear complex of the barn owl. *J Comp Neurol* 274: 212–238, 1988b.

**Takahashi TT, Wagner H, Konishi M.** Role of commissural projections in the representation of bilateral auditory space in the barn owl's inferior colliculus. *J Comp Neurol* 281: 545–554, 1989.

**von Campenhausen M, Wagner H.** Influence of the facial ruff on the sound-receiving characteristics of the barn owl's ears. *J Comp Physiol A* 192: 1073–1082, 2006.

**Vonderschen K, Wagner H.** Tuning to interaural time difference and frequency differs between the auditory arcopallium and the external nucleus of the inferior colliculus. *J Neurophysiol* 101: 2348–2361, 2009.

**Vonderschen K, Wagner H.** Transformation from a pure time delay to a mixed time and phase delay representation in the auditory forebrain pathway. *J Neurosci* 32: 5911–5923, 2012.

**Wagner H, Brill S, Kempter R, Carr CE.** Microsecond precision of phase delay in the auditory system of the barn owl. *J Neurophysiol* 94: 1655–1658, 2005.

**Wagner H, Brill S, Kempter R, Carr CE.** Auditory responses in the barn owl's nucleus laminaris to clicks: impulse response and signal analysis of neurophonic potential. *J Neurophysiol* 102: 1227–1240, 2009.

**Wagner H, Takahashi T, Konishi M.** Representation of interaural time difference in the central nucleus of the barn owl's inferior colliculus. *J Neurosci* 7: 3105–3116, 1987.

**Wang Y, Karten HJ.** Three subdivisions of the auditory midbrain in chicks (*Gallus gallus*) identified by their afferent and commissural projections. *J Comp Neurol* 518: 1199–1219, 2010.

**Yin TC, Chan JC.** Interaural time sensitivity in medial superior olive of cat. *J Neurophysiol* 64: 465–488, 1990.

**Zhou Y, Carney LH, Colburn HS.** A model for interaural time difference sensitivity in the medial superior olive: interaction of excitatory and inhibitory synaptic inputs, channel dynamics, and cellular morphology. *J Neurosci* 25: 3046–3058, 2005.